CSIRO PUBLISHING

International Journal of Wildland Fire **2016**, *25*, 90–101
http://dx.doi.org/10.1071/WF14173

Fire weather conditions and fire–atmosphere interactions observed during low-intensity prescribed fires – RxCADRE 2012

Craig B. Clements[A,I], *Neil P. Lareau*[A], *Daisuke Seto*[A], *Jonathan Contezac*[A], *Braniff Davis*[A], *Casey Teske*[B], *Thomas J. Zajkowski*[C,D], *Andrew T. Hudak*[E], *Benjamin C. Bright*[E], *Matthew B. Dickinson*[F], *Bret W. Butler*[G], *Daniel Jimenez*[G] *and J. Kevin Hiers*[H]

[A]Fire Weather Research Laboratory, Department of Meteorology and Climate Science, San José State University, San José 95192, CA, USA.
[B]College of Forestry and Conservation, National Center for Landscape Fire Analysis, The University of Montana, Missoula, MT 59812, USA.
[C]USDA Forest Service, Remote Sensing Applications Center, Salt Lake City, UT 84119, USA.
[D]Present address: Institute for Transportation Research and Education, North Carolina State University, Centennial Campus, Raleigh, NC 27695, USA.
[E]USDA Forest Service, Rocky Mountain Research Station, Forestry Sciences Laboratory, Moscow, ID 83843, USA.
[F]USDA Forest Service, Northern Research Station, 359 Main Road, Delaware, OH 43015, USA.
[G]USDA Forest Service, Fire Sciences Laboratory, Missoula, MT 59808, USA.
[H]Wildland Fire Center, US Air Force, Eglin Air Force Base, Niceville, FL, USA.
[I]Corresponding author. Email: craig.clements@sjsu.edu

Additional keywords: Doppler lidar, micrometeorology.

Received 25 September 2014, accepted 14 September 2015, published online 1 December 2015

Introduction

The role of fire–atmosphere coupling on fire behaviour is not well established, and to date few field observations have been made to investigate the interactions between fire spread and fire-induced winds. Therefore, comprehensive field observations are needed to better understand micrometeorological aspects of fire spread. To address this need, meteorological observations were made during the Prescribed Fire Combustion and Atmospheric Dynamics Research Experiment (RxCADRE) field campaign using a suite of meteorological instrumentation to measure both the ambient fire weather conditions and the fire–atmosphere interactions associated with the fires and plumes. Fire–atmosphere interactions are defined as the interactions between presently burning fuels and the atmosphere, in addition to interactions between fuels that will eventually burn in a given fire and the atmosphere (Potter 2012).

Currently, much of the meteorological sampling for fire behaviour applications and science is performed at a very coarse resolution (i.e. hundreds of metres to kilometres), such as that from standard remote automated weather station networks in existence throughout the United States (Horel and Dong 2010). However, there is an increasing need to measure fire–atmosphere interactions at finer scales to better understand the role of near-surface wind and thermodynamic structures of fire behaviour (Clements *et al.* 2007; Clements and Seto 2015). An ancillary need for these measurements is to provide evaluation datasets for new-generation coupled fire–atmosphere modelling systems (Coen *et al.* 2013; Filippi *et al.* 2013; Kochanski *et al.* 2013).

To date, few field experiments have focussed on the simultaneous measurement of fire behaviour and fine-scale meteorology. The FireFlux experiment (Clements *et al.* 2007, 2008; Clements 2010) provided the first dataset of *in situ* micrometeorological measurements during a fire front passage (FFP). Although the FireFlux dataset remains the standard for the evaluation of coupled fire–weather models (e.g. Filippi *et al.* 2013; Kochanski *et al.* 2013), it is limited by a lack of comprehensive fire behaviour measurements. Therefore, more comprehensive field experiments are required to better understand the role of fire–atmosphere interactions on fire spread. To that end, an extensive set of meteorological instruments was deployed in order to obtain a comprehensive suite of fire behaviour measurements that included multiple airborne and *in situ* ground-based platforms.

The goal of this paper is to describe the overall meteorological measurement campaign design and methods and present some initial results from analyses of two burn experiments. The paper is organised as follows: experimental design and instrumentation

Table 1. Meteorological instrumentation used in RxCADRE

v_r, radial velocity; β, aerosol backscatter intensity; CSU-MAPS, California State University – Mobile Atmospheric Profiling System; *u* horizontal streamwise velocity; *v*, horizontal cross-stream velocity; *w*, vertical velocity; T_s, sonic temperature; *T*, air temperature; *Q*, total heat flux, Q_r, radiative heat flux, *RH*, relative humidity; *WS*, wind speed; *WD*, wind direction

Platform	Sensor type and model	Variables	Measurement height (m AGL)	Sampling frequency
Micrometeorology tower	3D sonic anemometer (Applied Technologies Inc. SATI Sx)	u, v, w, t_S	2.0 and 5.8 (3.8 and 8.7 for L2F)	10 Hz
	Type-E thermocouples (Omega Inc. 5SC-TT-E)	T	1.0–6	5 Hz
	Total heat flux (Hukseflux SBG01)	Q (kW m^{-2})	2.8	5 Hz
	Radiative heat flux (Medtherm 64 series)	Q (kW m^{-2})	2.7 (8.3 for L2F)	5 Hz
CSU-MAPS 32-m extendable tower	Thermistor–hygristor sensors (Vaisala, Inc. HMP45C)	T, RH	7.0–31.0	1 min
	3D sonic anemometers (RM Young 81000), 2D anemometers (Gill, WindSonic)	u, v, w, t_S, u, v	7.0 and 31.0 7.0–31.0	10 Hz, 1 Hz
Doppler mini SoDAR	(Atmospheric Research and Technology VT-1)	u, v, w	15.0–200	1 Hz
CSU-MAPS mobile profilers	Doppler lidar (Halo Photonics, Ltd, Streamline 75)	v_r, β	3; range gate: 18	1 Hz
	Microwave profiler (Radiometrics Corp., MP-3000A)	T, RH	50–1 × 10^4	180 s
Cup-and-vane anemometers	Wind speed and direction (Onset Computer Corporation, S-CA-M003)	Wind speed and direction	3.3	3 s

used, results from one of the small burn units (S4) and one of the large burn units (L2G), and conclusions and summary.

Experimental design and instruments

The RxCADRE meteorological measurement campaign consisted of a variety of measurement platforms and instrument types. The experimental design was aimed at measuring both the ambient meteorological conditions surrounding each burn plot and the *in situ* fire–atmosphere interactions within the burn plots. Table 1 lists each instrument used for meteorological measurements. The wind field was measured extensively using several instruments and platforms, including a scanning Doppler wind lidar, an array of cup-and-vane anemometers around each burn unit perimeter, an interior tower equipped with two sonic anemometers (Fig. 1*a*), a Doppler mini-Sodar wind profiler, and a portable, 30-m meteorological tower (Fig. 1*b*) placed outside each burn unit (model 5SC-TT-E-40, Omega Engineering, Stamford, CT) (except during the L1G burn on 3 November 2012, where the tower was placed in the middle of the burn unit). Table 2 lists cup-and-vane anemometer spacing and ignition information for each burn unit.

The CSU-MAPS

The California State University – Mobile Atmospheric Profiling System (CSU-MAPS) was deployed during the entire field campaign (Fig. 1*c*). The CSU-MAPS consists of several platforms and sensor types including a scanning Doppler lidar, microwave temperature and humidity profiler and surface weather station, all mounted on a Ford F-250 4 × 4 truck. In addition to the remote-sensing platforms, a portable 30-m meteorological tower mounted on a dual-axle trailer (Fig. 1*b*) was equipped at four levels with thermistor–hygristor probes to measure temperature and humidity (HMP-45C, Vaisala Inc., Vantaa, Finland) and 2D sonic anemometers (Gill Windsonic, New Milton, UK). Additionally, two 3D sonic anemometers (model 81000, RM Young, Traverse City, MI) were mounted

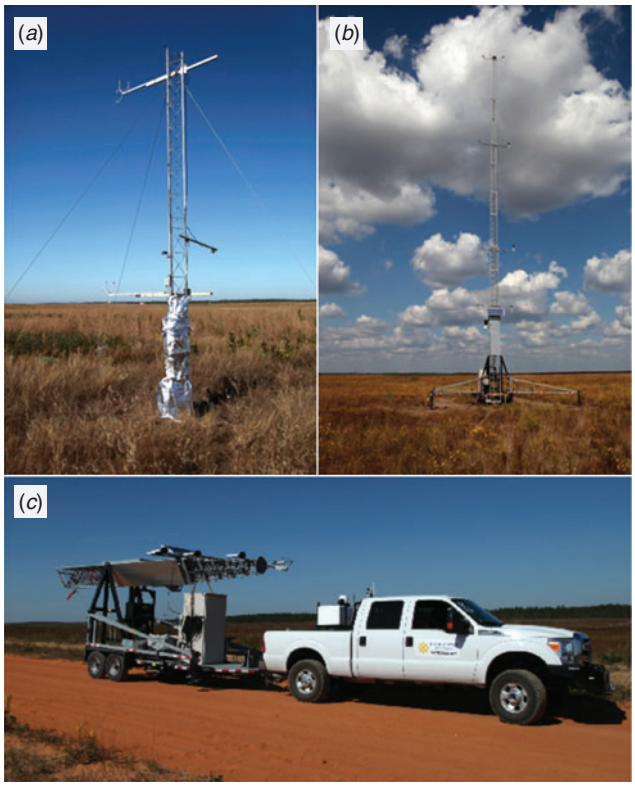

Fig. 1. Photographs of (*a*) 6-m micrometeorological tower; (*b*) CSU-MAPS (California State University – Mobile Atmospheric Profiling System) tower deployed within L1G burn unit; and (*c*) complete CSU-MAPS system.

on the tower at 7 and 31 m above ground level (AGL). A more detailed overview of the CSU-MAPS is provided in Clements and Oliphant (2014).

The key instrument of the CSU-MAPS is a pulsed Doppler lidar (model Streamline 75, Halo Photonics Ltd, Worcestershire,

Table 2. Burn plot instrumentation and ignition information
HIP, highly instrumented plot

Burn unit	Number of anemometers	Burn date (2012)	Burn start time (UTC)	Data collection end time (UTC)
S6	10 adjacent to plot (test plot)	31 October	1911	2000
S4	40 adjacent to plot; 3 NW of plot	1 November	1935	2115
S5	32 adjacent to plot; 3 NW of plot	1 November	1810	1930
L1G	76 adjacent to plot	4 November	1831	2359
S7	33 adjacent to plot; 3 NW of plot	7 November	1725	1850
S8	25 adjacent to plot	7 November	2016	2130
S9	23 adjacent to plot	7 November	1854	2010
L2F	34 adjacent to plot; 1 at each HIP; 12 crossing interior firebreak	11 November	1802	2359
L2G	35 adjacent to plot; 1 at each HIP; 12 crossing interior firebreak	10 November	1823	2359

UK). The lidar emits an eye-safe infrared laser at a wavelength of 1.5 μm (Pearson *et al.* 2009, 2010). The system is equipped with an all-sky optical scanner, enabling the lidar to scan from 0 to 360° in azimuth angle and −15° to 195° in elevation angle. The range gate is 18 m with a minimum range of 80 m and a potential maximum range of 9.6 km, typically associated with heavy aerosol targets such as clouds or smoke. The lidar measures radial velocities along the path of the beam and the attenuated backscatter (hereafter just backscatter). The backscatter is highly sensitive to micron-sized aerosol and thus provides detailed measurement of the smoke distribution during each scan. The CSU-MAPS is also equipped with a microwave temperature and humidity profiler that provides a continuous sounding from the surface to 10 km AGL by observing atmospheric brightness temperatures in 21 K-band channels and 14 V-band channels (Ware *et al.* 2003). Data from the microwave profiler are not discussed in the present paper. Upper-air soundings were made using radiosondes (Vaisala, Inc., RS-92GPS) that were launched on site just before and after each burn period.

Doppler mini SoDAR

A model VT-1 (Atmospheric Research & Technology LLC, Kailua-Kona, HI) Doppler mini SoDAR was used to characterise the surface-layer wind profile.

Surface anemometer array

A network of surface cup-and-vane anemometers was set up with ~20-m spacing around each small burn block, with adjacent burn-block edges sharing anemometers. These instruments were mounted 3.3 m AGL. The data are used to characterise surface flow patterns before and during the burns. Cup revolutions and unit vector components were sampled at a frequency of 1 s. Wind speed is the average speed for the entire logging interval. Gust speed is the highest 3-s wind recorded during the logging interval. Average direction is calculated from the average of the vector components. The three large burn blocks were also instrumented with cup-and-vane anemometers at 150- or 300-m spacing around the perimeters. Three highly instrumented plots (HIPs) were placed within each of the large burn blocks, and each of the HIPs had an anemometer located nearby (within the burn unit) in plots L2F and L2G. In addition to the standard spacing, all of the large burn blocks had additional anemometers placed to capture wind variability. Block L1G had a concentration of anemometers spaced ~50 to 75 m apart around the east corner to attempt to capture surface-layer flow variability due to canopy effects (Fig. 2). Additionally, anemometers were placed approximately perpendicular to the interior firebreak road between L2F and L2G, with three on each side of the road, to assess the effects of the canopy on surface flow.

Micrometeorological measurements

To capture the near-surface micrometeorology of the passing fire front, a guyed steel tower instrumented with anemometers, thermocouples and heat flux sensors was deployed inside each of the nine burn units; the tower was 9.1 m tall for the forested burn unit (L2F) and 6.1 m for all other burn units. Two 3D sonic anemometers (SATI Sx probe, Applied Technology Inc., Longmont, CO) were mounted at the height of 5.8 and 2.0 m AGL (8.7 and 3.8 m AGL for L2F). An array of fine-wire thermocouples (model 5SC, Type-E, Omega Inc., Stamford, CT) was used to measure plume and near-surface temperature profiles. The thermocouples were placed every metre from 1 m AGL to the top of the towers. Total and radiative heat fluxes were measured using a Schmidt-Boelter gauge total heat flux sensor (model SBG01, HukseefluxUSA Inc., Manorville, NY) and a Gardon gauge radiant heat flux sensor (model 64P-50–24, Medtherm, Huntsville, AL), respectively. All tower data were recorded using a Campbell Scientific, Inc. CR3000 datalogger mounted near the base of the tower housed in an environmental enclosure, and the tower bases were protected from the extreme heat of the fire using fire-shelter material. The fire front was allowed to burn directly underneath the towers.

Fire perimeter and fire radiant energy measurements

The RxCADRE project offered the opportunity to assess capabilities of small remotely piloted aircraft systems (RPAS), also known as unmanned aircraft systems (UAS), in the context of prescribed fire operations (Dickinson *et al.* 2015; Zajkowski *et al.* 2015). The latter papers contain more detail about the collection and processing of the imagery. The perimeters used for the S4 burn block were created from thermal imagery from an oblique mounted Tau 640 (FLIR, Wilsonville, OR) flown on a G2R RPAS orbiting the plot at 180 m AGL. The thermal

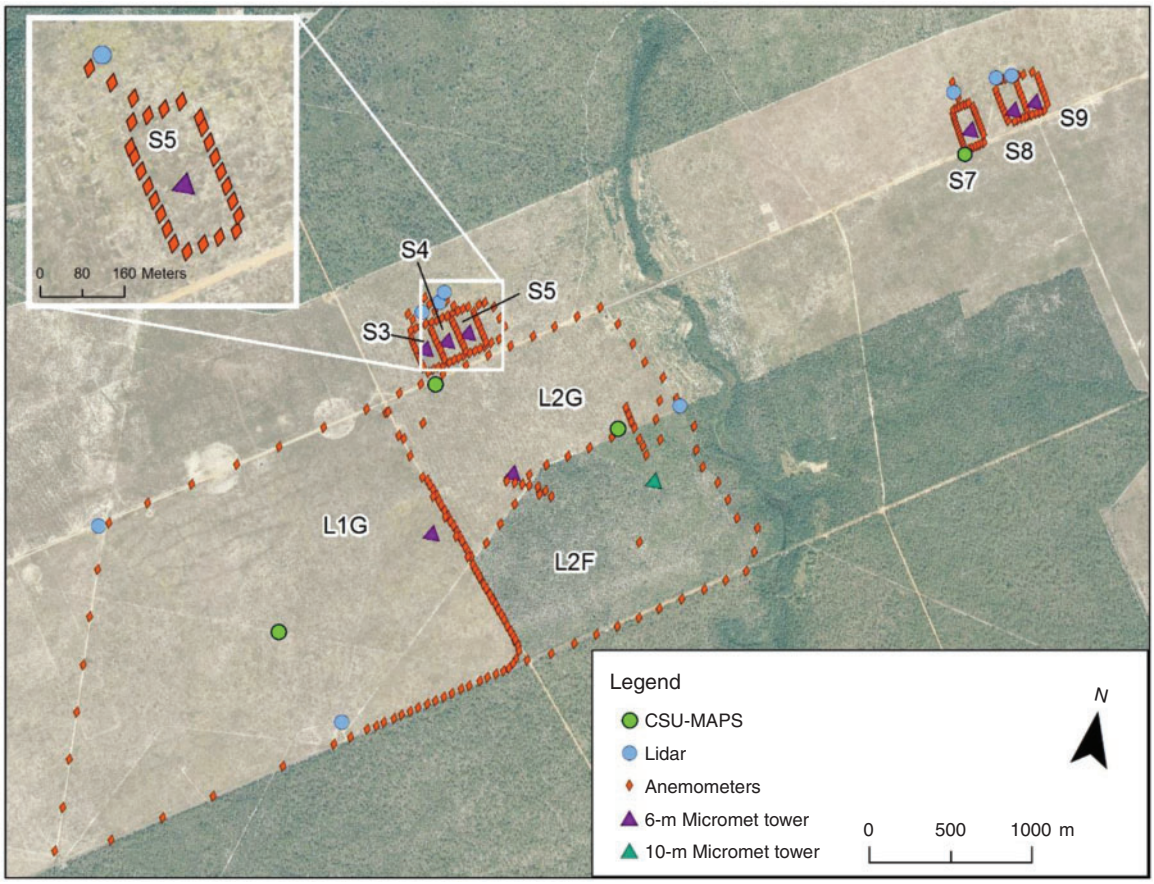

Fig. 2. Map showing details of burn plots and main meteorological instrument locations. Burn plots are named as small (S) plots and large (L) plots.

imagery was orthorectified using the *Sarnoff TerraSight* software package (SRI International, Menlo Park, CA), using features visible on the imagery and high-resolution orthophotos, and 'hot targets' (cans of burning charcoal) placed at surveyed locations. The fire perimeters were derived manually in ESRI *ArcMap* utilising imagery with a consistent look angle to correct for parallax. This constraint limited the interval between perimeters to ~2 min. The perimeters and fire radiative energy from the L2G burn were measured using the Wildfire Airborne Sensor Program (WASP) sensor on a fixed-wing aircraft (Dickenson *et al.* 2015; Kremens and Dickinson 2015). These observations are coupled with the lidar radial velocity measurements for analysis and discussion and are presented below.

Observations and results

In this section, we describe the synoptic environment and boundary-layer evolution of each burn day. In addition, preliminary results from the S4 and L2G burn blocks illustrating key measurement platform performance and some observed fire–atmosphere interactions are discussed. A full analysis of all the observations of fire–atmosphere interactions is beyond the scope of this overview paper, but will be presented in future studies combining modelling and observations.

Large-scale weather patterns associated with experimental burns

The controlled burns were conducted from mid-morning (~1600 Coordinated Universal Time (UTC)) through early afternoon (~2200 UTC) on 1, 4, 7, 10 and 11 November 2012. The large-scale patterns of wind, temperature and pressure affecting northern Florida during each burn are summarised in this section (Fig. 3). We also examine pre- and post-burn changes to the atmospheric profile using radiosonde data (Fig. 4) and discuss the average surface weather conditions at the time of ignition, which are summarised in Table 3. Data from the European Centre for Medium-Range Weather Forecasts (ECMWF) Re-Analysis (ERA)-Interim are used to produce the synoptic analyses in the present study (Dee *et al.* 2011). The ERA-Interim uses the ECMWF integrated forecasting system and a four-dimensional variational data assimilation system that ingests observations within a 12-h window around the analysis time.

Post-frontal burns under north, north-westerly winds

Burns S3–S5 and S7–S9 on 1 and 7 November respectively were conducted under the influence of upper-level troughs in a post-frontal air mass characterised by northerly winds and deep convective boundary layers.

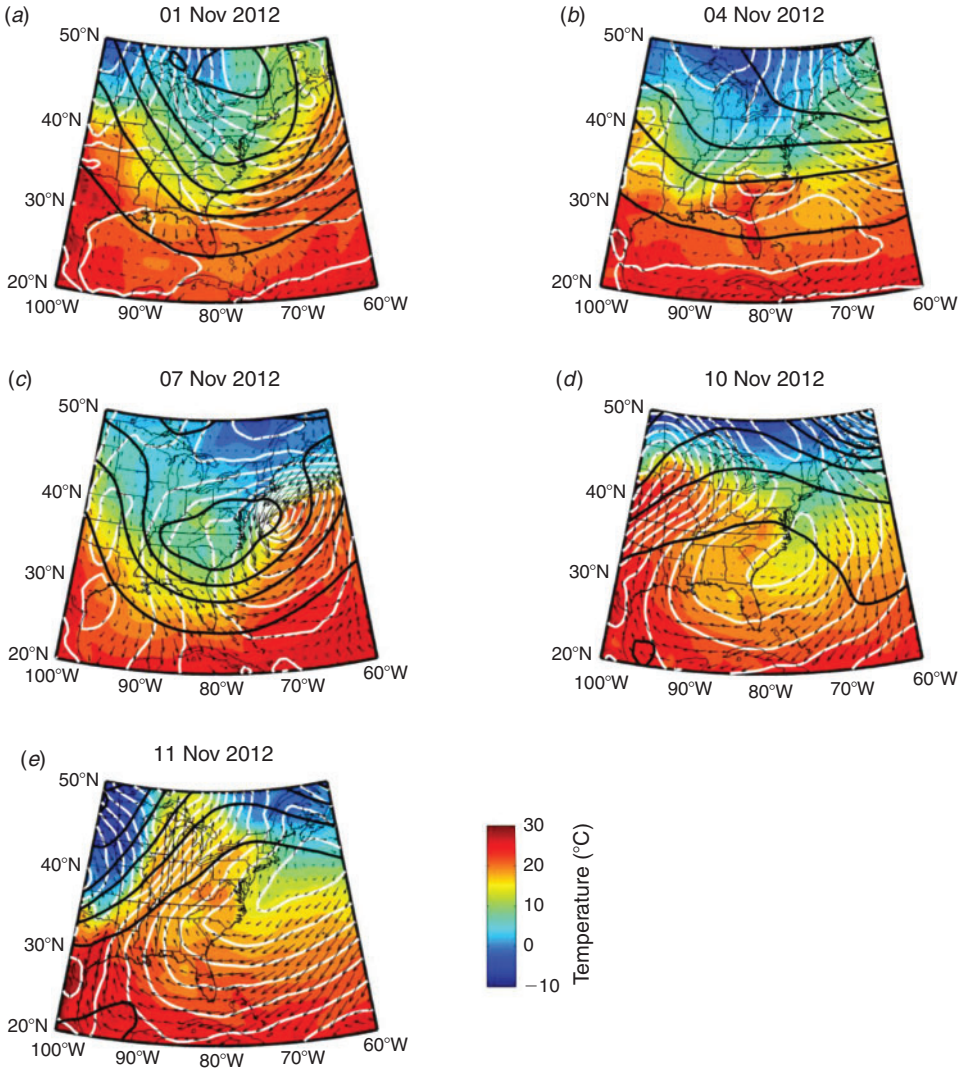

Fig. 3. Synoptic-scale weather conditions during each controlled burn. Each panel shows the 500-hPa geopotential height (black contours, 100-m contour interval), the 1000-hPa geopotential height (white contours, 25-m contour interval), the 2-m air temperature (colour shading) and the 10-m wind vectors. Plots burned on each day are: (*a*) S3, S4 and S5; (*b*) L1G; (*c*) S7, S8 and S9; (*d*) L2G; and (*e*) L2F.

Specifically, during burns S3–S5, a high-amplitude upper-level trough over the eastern United States generated a north to north-west flow with weak cold advection (Fig. 3*a*). The northerly flow was apparent in the morning (1641 UTC) and afternoon (2015 UTC) profiles (Fig. 4*a*). The morning profile indicated a shallow mixed layer extending from the surface to ~500 m where an isothermal capping layer resided. By afternoon, this capping layer was removed and a deep dry adiabatic profile extended upwards to ~1700 m ASL (above mean sea level), providing good ventilation during the burn period.

Similarly, during the third day of controlled burns (7 November, S7–S9), another long-wave trough affected the eastern US. The upper-level trough was accompanied by a surface cyclone near Chesapeake Bay (Fig. 3*c*) and an associated cold front was located east of Florida, generating strong north-west flow across the burn region.

The soundings for 7 November, for example, revealed deep north-west flow in the post-cold-frontal air mass (Fig. 4*c*). The morning profile indicated a mixed layer extending from the surface to ~1500 m ASL, which was atypically deep for that time of day owing to the destabilisation of the post-frontal air mass. By afternoon, the mixed layer warmed and increased in depth to ~1800 m ASL.

Prefrontal burns during westerly winds

Burn L1G on 4 November was conducted as a low-amplitude upper-level trough was situated over the Ohio River Valley with an associated region of weakly organised surface low pressure over South Carolina (Fig. 3*b*). Moderate west to north-west flow affected the region near the burn site as a cold front accompanying the surface low approached from the north-west.

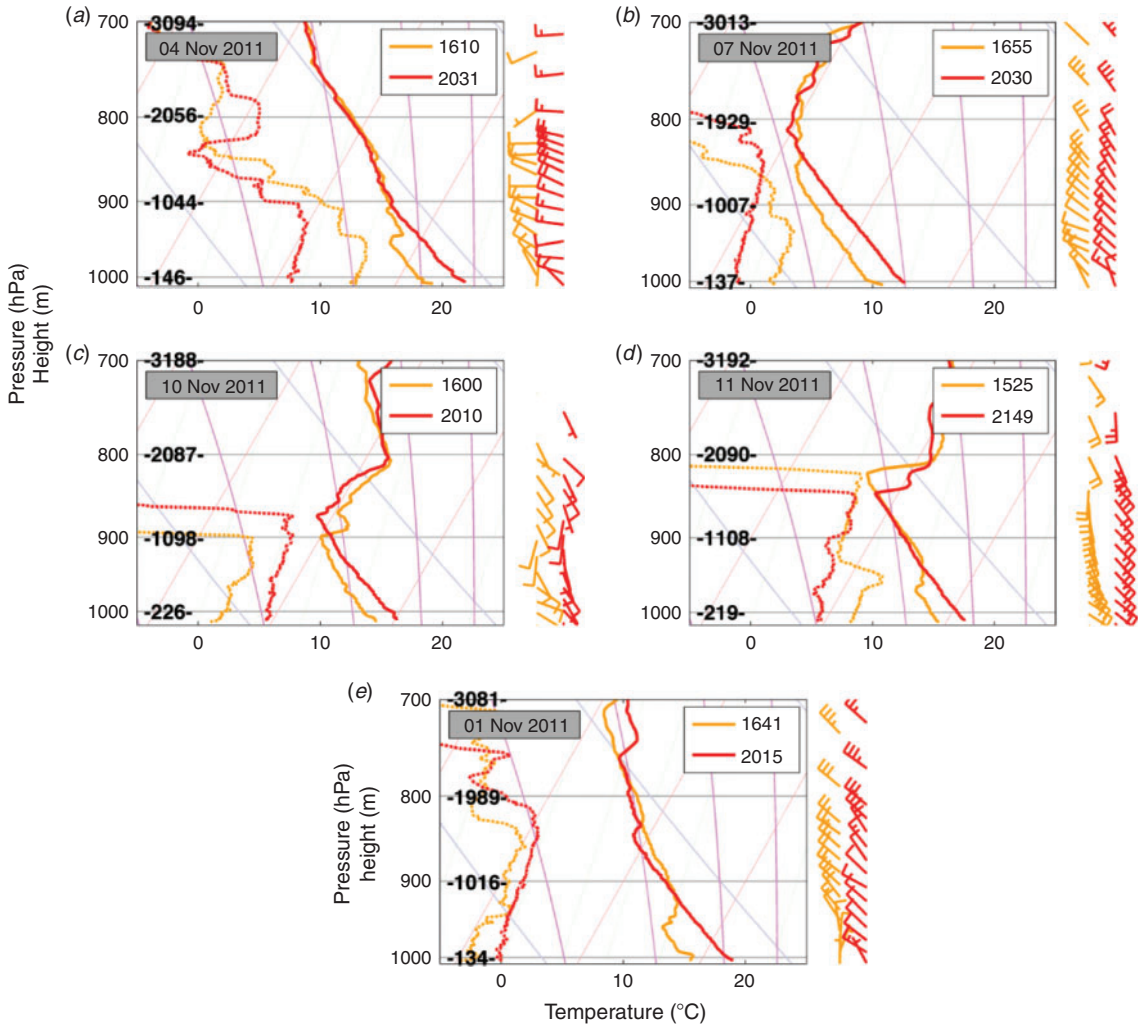

Fig. 4. Skew-T log P diagrams (where P is atmospheric pressure) for the pre-fire (orange) and post-fire (red) radiosondes for each burn day (*a* through *e*). Each panel shows the air temperature (solid lines), dew-point temperature (dashed lines) and the wind profile (barbs). Times are in UTC and height is metres above mean sea level.

Table 3. Average meteorological surface conditions at ignition

Burn unit	Temperature (°C)	Relative humidity (%)	Wind speed (m s^{-1})	Wind direction (°)
S3, S4, S5	22	28	4.0	345
S7, S8, S9	17	50	3.5	300
L1G	26	50	2.0	320
L2F	24	60	3.0	130
L2G	23	41	2.0	130

The morning sounding (Fig. 3*b*), taken at 1610 UTC (1010 Local Standard Time (LST)), indicated a surface-based mixed layer extending to a depth of ~600 m ASL. The top of the mixed layer was delineated by a capping inversion across which temperature increased and dewpoint decreased sharply. Above the capping layer, a nearly adiabatic residual layer extended upward to ~1000 m ASL. By late afternoon, surface-based mixing eroded through the capping inversion, coupled with the residual layer and substantially increased the mixing depth. Winds throughout the day were from the west-north-west.

Burns under the influence of high pressure and south-easterly winds

The final two burns, L2G and L2F on 10 and 11 November respectively, were conducted under the influence of high pressure (Fig. 3*d*, 3*e*). On 10 November, the axis of an upper-level ridge was positioned over the eastern US, with the centre of surface high pressure off the North Carolina coast. This configuration generated weak easterly flow across northern Florida. The following day, 11 November, the upper ridge and surface anticyclone shifted to the east as a trough slowly approached from the west. The wind across the Florida panhandle increased from the south-east, driving a warm moist onshore flow.

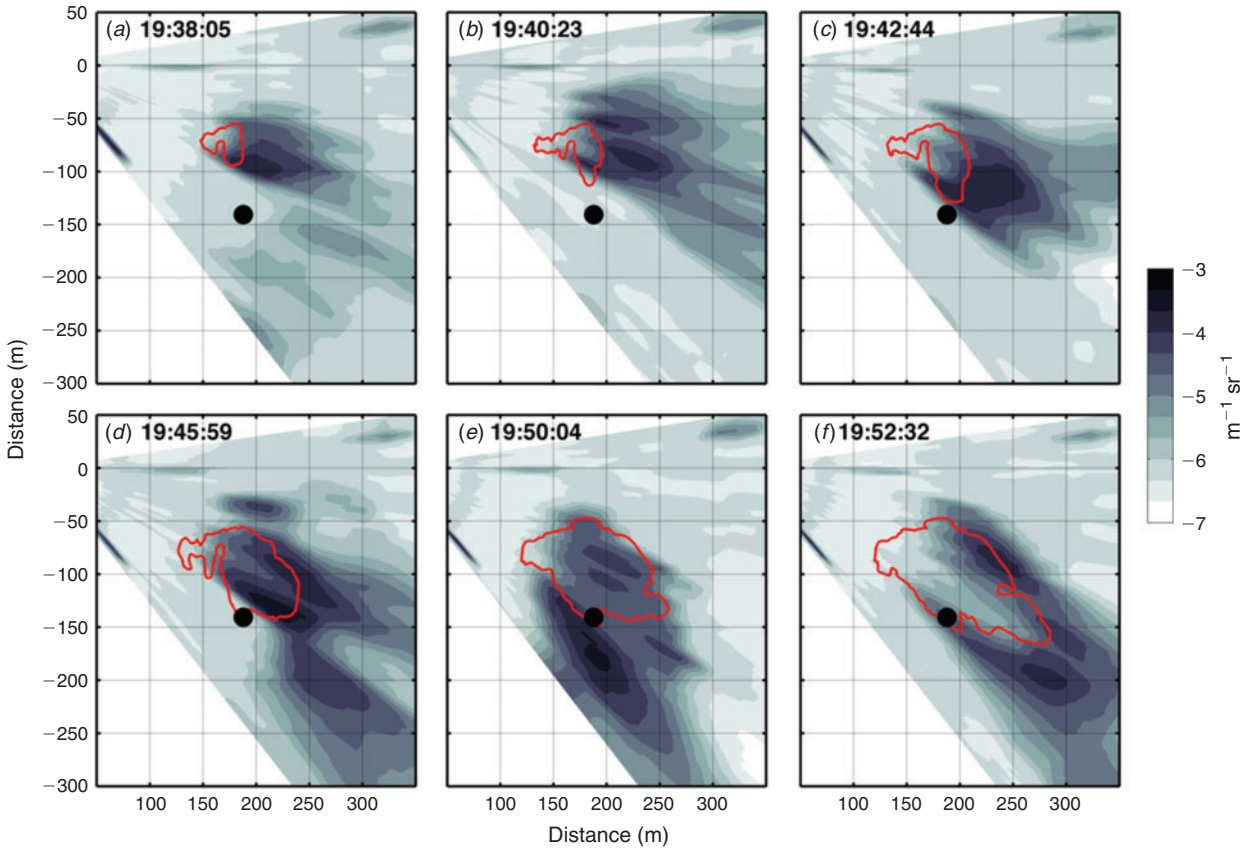

Fig. 5. Lidar smoke observations (attenuated backscatter (m^{-1} sr^{-1}), grey shading is proportional to smoke concentration) and fire perimeter (red contour) during the S4 burn. Micrometeorological tower is indicated by solid circle. Each panel represents a 30-s time average of the backscatter centred on the time listed above each figure column. Time is in UTC.

The soundings on 10 November indicated a sharp subsidence inversion associated with the upper-level ridge (Fig. 3*d*). The inversion was apparent as a layer of warm and very dry air aloft. At 1600 UTC (1000 LST), the base of this layer was situated at ~1100 m ASL. Later in the afternoon, the convective boundary layer eroded upward into the capping layer, increasing the mixing depth to ~1300 m ASL. The winds throughout the mixed layer were from the east and south-east at 2–5 m s^{-1}.

On 11 November, as on the previous day, the subsidence inversion was a key feature of both the morning and afternoon soundings (Fig. 4*e*). The morning sounding showed an additional stable layer at ~500 m, marking the remnants of the nocturnal decoupling. By afternoon, convection had eroded through this intermediary capping layer and coupled with the residual layer aloft, allowing convective mixing up to ~1800 m ASL. Winds throughout the period were strong from the south-east, consistent with the increased flow around the departing anticyclone.

Doppler lidar observations

The scanning Doppler lidar was used during each experimental burn to measure the spatial variability of the wind field and the characteristics of the smoke plume. A plan position indicator (PPI) scan was used to collect radial velocities and aerosol backscatter data across predetermined horizontal sectors covering the burn plots following Charland and Clements (2013).

The lidar was placed on the upwind side of the perimeter of burn plots S4 and L2G in optimised locations that allowed the laser to be mostly uninterrupted by terrain, foliage and instrumentation. However, this strategy did have limitations, because at times the lidar beam was not able to penetrate through the densest part of the plume, thus restricting observations of flows on the downwind side of the plume. The range of the lidar was ~1000 m for most experiments with a gate length of 18 m.

S4 burn plot

During the S4 burn, the lidar performed PPI sector scans between 80° and 140° azimuths at an elevation angle of 2°. As such, the dominant north-westerly wind was well aligned with centre of the lidar sector scan.

Fig. 5 provides an overview of the lidar logarithmic backscatter during the S4 burn along with the fire perimeter. The backscatter is highly sensitive to smoke particles (e.g. $PM_{2.5}$), and thus shows the spatial distribution and relative concentration of smoke rising from both the flaming front and the smouldering portions of the fire. The data were averaged for the 30-s interval centred on the fire perimeter observation time, which is shown above each column of Fig. 5. The fire perimeter

itself was determined from IR imagery as described above (Zajkowski *et al.* 2015).

The lidar backscatter data are aligned with the observed fire perimeter and generally show that the largest smoke concentrations were advected downwind of the advancing portions of the fire. This observation is consistent with the north-westerly background wind flowing through the fire front. However, the data also show subtle, albeit important, shifts in the mean direction of the smoke spread and the corresponding advance of the fire. For example, comparing and contrasting panels (*b*) through (*e*) in Fig. 5 – direction of smoke spread, location of heaviest smoke concentration and most active portion of the fire front – indicate a wind shift from westerly (Fig. 5*b*) to more northerly (Fig. 5*e*). In fact, the intensity of the smoke backscatter and change in fire perimeter suggest that during the wind shift, the most active portion of the fire changes from the broad eastern flank to the more complex southern flank (compare panels (*c*) and (*e*)).

The fire and associated smoke plume subsequently made a significant advance to the south-east and assumed an elongated parabolic shape characteristic of head fires (Fig. 5*f*). A notable feature in the backscatter data during the head fire advance was a slot of clear air that extended from the backing edge of the fire into the advancing fire front, suggestive of an inflow jet (Fig. 5*f*).

To inspect the head fire development in more detail, the lidar-derived radial wind velocity data are shown in Fig. 6, corresponding to the smoke backscatter in panels (*d*)–(*f*) of Fig. 5. The radial velocity is the projection of the full wind vector onto the lidar radial. It is immediately apparent from the data that a significant increase in wind speed and flow organisation corresponded to the onset of the head fire advance (Fig. 6*c*). For example, a 3–4.5-m s^{-1} flow was aligned with the radial along the centreline of the fire parabola. The increased flow extended from upwind of the fire, through the fire front and into the rising smoke plume. The strongest instantaneous winds during this period were ~7 m s^{-1} (not shown). By comparison, during the two previous time intervals when the fire spread was more complex, the flow was considerably weaker and less well organised (Fig. 6*a*, *b*). It is interesting that a significant fire-induced wind was not present during the early stages of the fire spread, but later developed, corresponding to the onset of a more characteristic head fire shape. These observations suggest a possible relationship between fire scale, both in terms of intensity and size, and the atmospheric response that leads to the positive feedback between fire propagation and fire-induced wind.

L2G burn plot

During L2G, the lidar was positioned on the south-east corner of the burn plot where it performed PPI scans between 240° and 320° azimuths at an elevation of 2°. In addition, to characterise the ambient wind affecting the fire evolution, the lidar made three vertical wind profiles during the 10 min before ignition, and these profiles were then averaged to provide a single profile of wind speed and direction (Fig. 7). The profile indicates weak wind shear in the lowest 200 m and constant south-easterly wind above, consistent with a well-mixed boundary layer and south-easterly synoptic-scale flow.

To gain perspective on the evolution of the L2G fire spread, fire-induced winds and smoke distribution, Fig. 8 combines lidar data and aircraft IR imagery. The displayed lidar data are post-processed to provide time maximum and time median values of smoke backscatter and radial velocity, respectively. These statistics are computed for the period ending at the time of the IR imagery, which is displayed in units of kilowatts per square metre and is a measure of both the fire shape and intensity (Dickinson *et al.* 2015; Hudak *et al.* 2015; Kremens and Dickinson 2015).

Shortly after ignition (~1827 UTC), the fire was confined along the four ignition lines, which were progressively laid down from the north-east to the south-west through the burn unit (left column, Fig. 8). The backscatter indicates that the smoke from each ignition line was swept from the south-east towards the north-west, approximately perpendicular to the fire front and aligned with the background wind. The radial velocity data during this time indicate that winds were initially light, with maximum values of ~2 m s^{-1}.

By 1832 UTC, small head-fire runs developed along portions of each fire line (second column, Fig. 8). By comparison, the backing fire progression was minimal. The individual head fires were each aligned with the south-easterly wind, as was the direction of smoke dispersion. Compared with earlier, it is now clear that the smoke plumes from the windward fire lines impinged on the downwind fire lines.

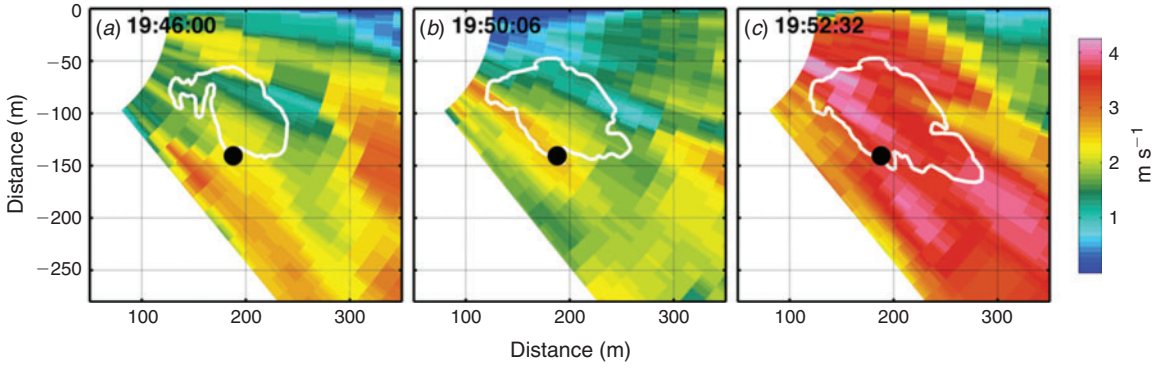

Fig. 6. Doppler radial velocity (m s^{-1}, shaded) and fire perimeter (white contour) during the later stages of the S4 burn. Micrometeorological tower is indicated by solid circle and time is in UTC.

Notably, compared with the wind speed near the time of ignition, a substantial fire-induced wind is evident, with median values in excess of 4 m s^{-1}. These data suggest that the maturing fire front caused an acceleration of the ambient winds into the leading fire line and extending through the downwind plume.

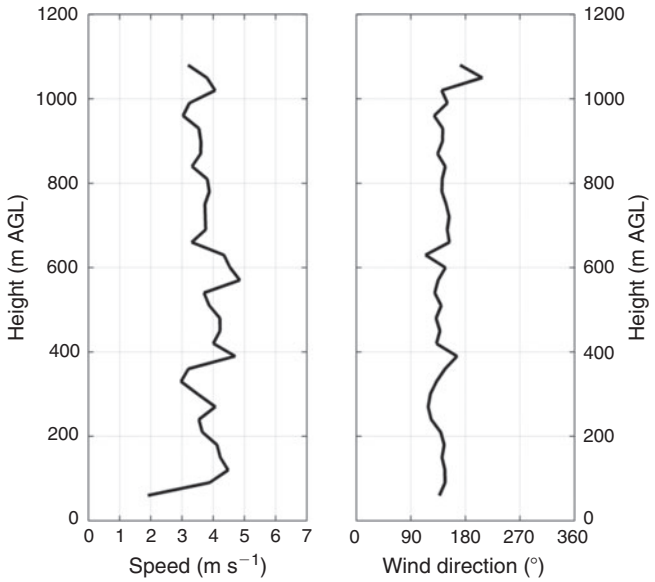

Fig. 7. Ten-minute mean vertical wind profile measured from the Doppler lidar before ignition at the L2G burn plot. Height is metres above ground level (m AGL).

These fire-induced winds appear to be strongest where the flow was aligned along the background wind (i.e. south-easterly) and where the fire was most mature (i.e. near the initial point of ignition).

As the ignition continued (Fig. 8*c*), the plume boundaries and fire lines began to merge as smoke and heat from each fire line were advected downwind. A continued fire-induced acceleration was apparent, with the flow speed increasing upstream of the leading fire line and reaching a maximum between the third and fourth fire lines. In addition, the most intense portion of the fire shifted south-westward. A commensurate south-westward shift in the radial of the maximum wind was observed (i.e. a more easterly component to the wind developed). This subtle wind shift was also evident in the IR data, which show the orientation of individual head runs aligning with the new fire-induced wind direction. Similar subtle wind shifts were observed during the S4 burn, and likewise affected the direction of fire propagation.

Collectively, these observations support the existence of a positive feedback process between fire-induced winds and fire spread. Although this feedback is well known, few observations to date provide spatially coherent and quantitative measures of fire-induced winds, such as are possible with the scanning Doppler lidar. Additional observations, and linked modelling studies, will be required to more fully understand these feedbacks and interactions.

Micrometeorology during fire front passage

S4 burn block

The evolution of the near-surface wind and turbulent heat fluxes of the fire front were measured using two 3D sonic

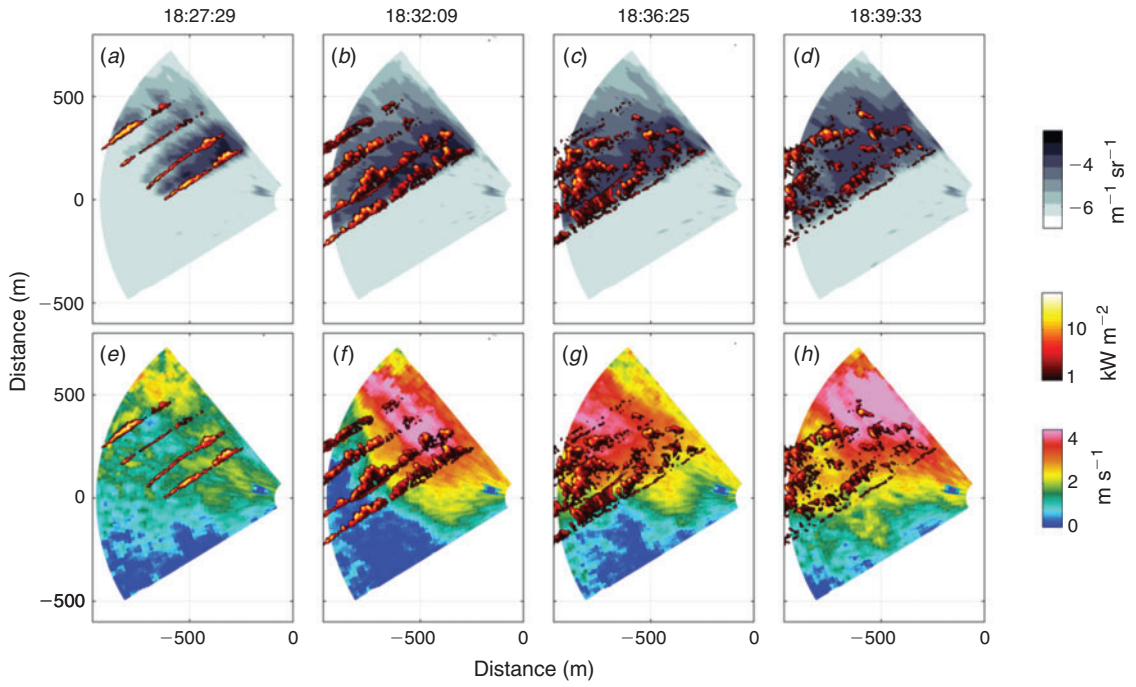

Fig. 8. Overview of L2G burn showing lidar data overlaid with infrared (IR) observations (log scale, kW m^{-2}) of the fire front. The top sequence (*a–d*) shows the maximum lidar backscatter (m^{-1} sr^{-1}) during the period ending at the time of the IR imagery (shown above each column), whereas the lower panels (*d–f*) display the median radial velocity (m s^{-1}).

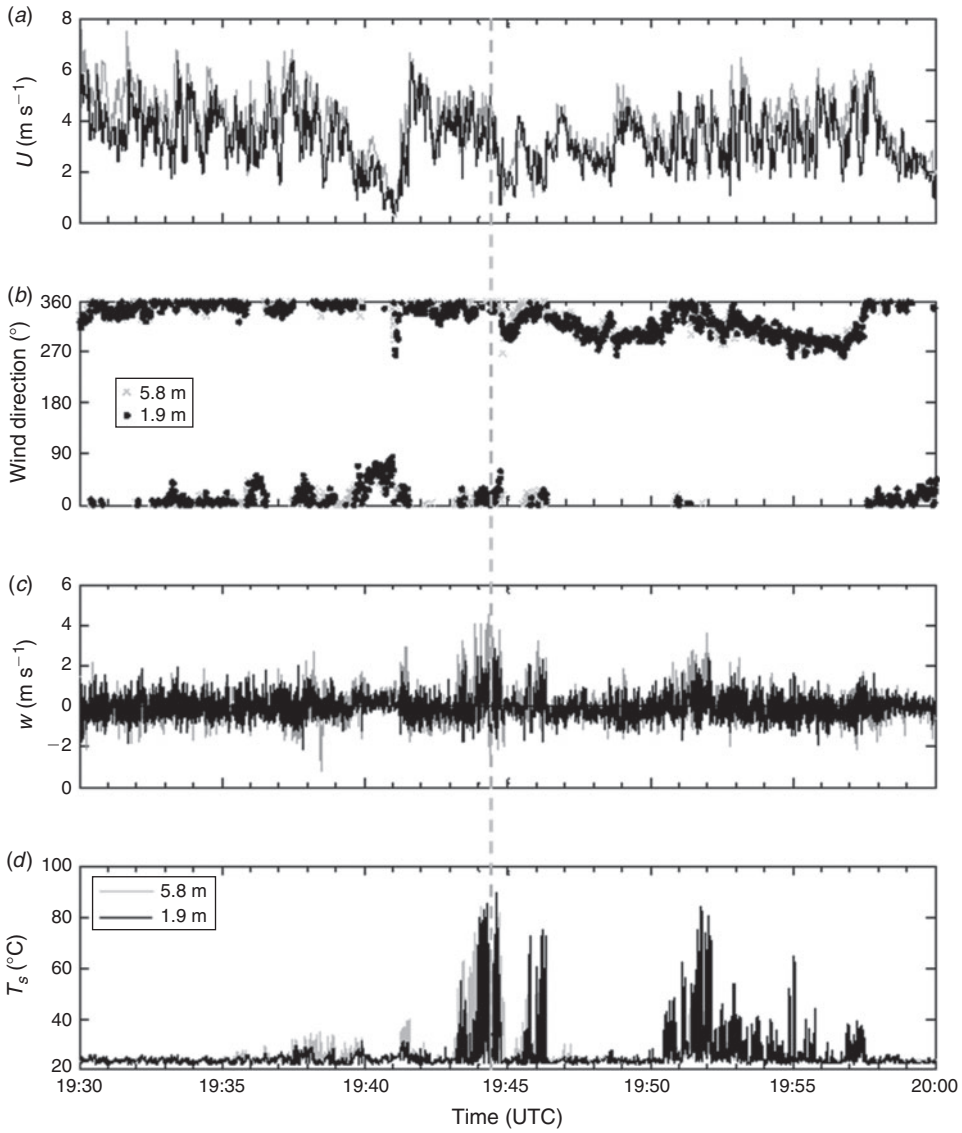

Fig. 9. Time series of 1-s averaged (*a*) horizontal wind velocity, *U*; (*b*) wind direction, °; (*c*) 10 Hz vertical wind velocity, *w*; and (*d*) 10 Hz sonic temperature, T_s measured during the S4 burn on 1 November 2012. The timing of the fire-front passage at the tower is indicated by the dashed vertical line and UTC is Coordinated Universal Time.

anemometers mounted on the *in situ* tower. Horizontal wind speed and direction, vertical velocities and sonic temperature were measured at 2.0 and 5.8 m AGL (Fig. 9*a–d*). The evolution of the fire front perimeter (Fig. 5) indicates that the FFP at the tower was at first (19:45:59 UTC) a head fire and later became more of a flanking fire (19:52:32 UTC). The time-series data in Fig. 9 indicate two periods of fire-front impacts, first with the head fire at 1944 UTC and second, the flank-fire period at 1952 UTC. In addition, the flank remained at the tower for a longer period, indicating a longer residence time compared with the head fire FFP. Although there are visually no signs of fire-induced flows ahead of the fire front (e.g. sudden changes in horizontal wind speed and direction) before 19:44:30 UTC, there is indication of a lull that occurred at 1941 UTC. At this time, the fire front was ~25 m upwind of the tower (Fig. 5*c*) and it is surprising that such a small fire and plume could modify the flow field in such a way, although weakly. Convective updrafts associated with the plume were also considerable given the small scale of the fire. Updraft velocities peaked to ~4 m s^{-1} at 5.8 m AGL. Strong downdrafts behind the fire line were not present as has been found in other and more intense experimental fires (e.g. FireFlux; Clements *et al.* 2007). This may be due to the fact that the fire and resulting convection were neither well-developed nor intense in the present study, limiting the fire–atmosphere coupling. In addition, because the main plume and head fire did not impact the tower, these flow features likely may not have been captured by the tower, but could have occurred at the head of fire. The wind direction turned to more westerly and north-westerly between 1945 and 1958 UTC (Fig. 9) as the fire perimeter reached the tower, possibly suggesting a more pronounced effect of fire-induced winds.

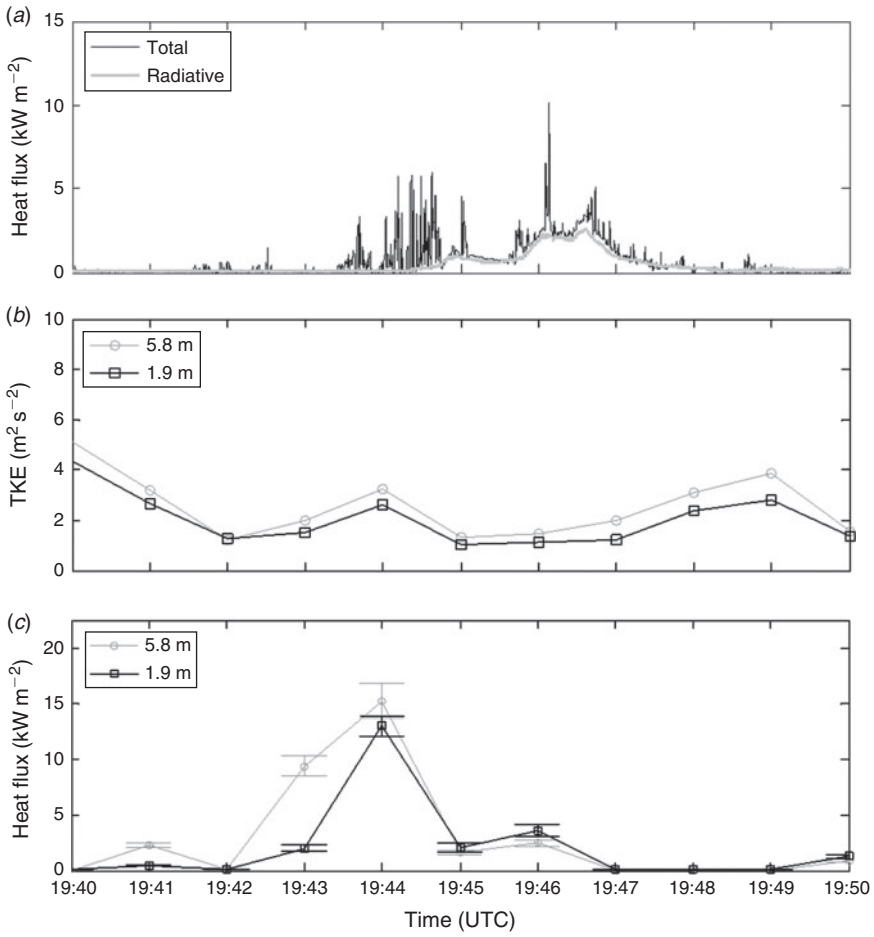

Fig. 10. Time series of (*a*) 10-Hz total and radiative heat flux; (*b*) 1-min averaged turbulence kinetic energy (TKE); and (*c*) sensible heat flux, measured during the S4 burn on 1 November 2012. Error bars indicate ±1 standard deviation.

Fig. 10*a* shows total and radiative heat flux measured at 2.7 m AGL at S4. A peak radiative flux value, incident on the sensor, of 2.6 kW m^{-2} was measured as the fire propagated beneath the tower and nadir-viewing sensors. Flame residence time was over 1 min as a result of a slow flanking fire. The low peak radiative heat flux value is similar to observations by Silvani and Morandini (2009), suggesting that the S4 fire was representative of a low-intensity fire. The 1-min averaged turbulence kinetic energy (TKE) increased only slightly from 2 to 3 $m^2 s^{-2}$ at both levels during the FFP even though the heat released from the fire front impacted the tower. The maximum 1-min averaged sensible heat flux, H_s, at 5.8 m AGL was 15.2, and 13.0 kW m^{-2} at 1.9 m AGL. The sensible heat flux represents the convective heating associated with the plume and not necessarily the heat transfer from the flame front to the fuels.

Summary and conclusions

The RxCADRE campaign represents a major effort in the simultaneous monitoring of fire weather and micrometeorology, with fine-scale fuels and fire behaviour sampling during multiple low-intensity prescribed-fire experiments. The experimental design was aimed at exploiting a high-spatial-resolution network of instrumentation to measure the small-scale meteorology within and around each burn block.

The scanning Doppler lidar provided high-resolution and large areal coverage of radial velocities across each burn block and was able to, for the first time, capture spatially resolved coherent flow structures coupled with airborne observations of fire perimeter and fire radiative intensity.

Results indicate that even low-intensity fires can induce fire–atmosphere coupling resulting in flow modification and perturbation of the fire front. This coupling is most likely associated with the plume and instabilities generated by the fire front. The low-intensity fires were generally associated with weak TKE, which did not change significantly above ambient during the FFP.

Observations from the larger burn, L2G, with a more complex multi-line head fire ignition pattern indicate that winds eventually doubled in strength as the plume boundaries and fire lines merged and the heat from each fire line was advected downwind. A subtle wind shift observed in the Doppler lidar

radial winds showed that the orientation of individual head fire runs aligned with the new fire-induced wind direction. This wind shift modified the head fire behaviour by shifting its direction with the local fire-induced wind and away from the mean ambient wind. These observations suggest that low-intensity prescribed fires are susceptible to small changes in wind direction and wind speed, often altering the fire spread. These changes may be a result of fire–atmosphere coupling induced by the fire itself or caused by the ambient turbulence regime and eddies associated with the atmospheric boundary layer present at the time of ignition.

In order to better understand how fire–atmosphere coupling affects fire behaviour, future studies should include a more extensive monitoring of atmospheric boundary layer properties upwind of experimental plots and also include more *in situ* measurements within the fire perimeter to better observe fire–atmosphere coupling and its influence on fire behaviour.

Acknowledgements

The authors would like to acknowledge many individuals from Eglin Air Force Base Jackson Guard who helped us meet our specific research goals, including Keith Hawk, David Grimm and Brett Williams, who was the overall incident commander for the experiments. In addition, we would like to acknowledge Wyndam Lewis and Richard Bagley for their help in the field. The meteorological measurement campaign was supported by funding from the Joint Fire Science Program (project no. 11–2-1–11) and the National Science Foundation (AGS-1151930).

References

Charland A, Clements CB (2013) Kinematic structure of a wildland fire plume observed by Doppler lidar. *Journal of Geophysical Research, D, Atmospheres* **118**, 3200–3212. doi:10.1002/JGRD.50308

Clements CB (2010) Thermodynamic structure of a grass fire plume. *International Journal of Wildland Fire* **19**, 895–902. doi:10.1071/WF09009

Clements CB, Oliphant AO (2014) The California State University – Mobile Atmospheric Profiling System (CSU-MAPS): a facility for research and education in boundary-layer meteorology. *Bulletin of the American Meteorological Society* **95**, 1713–1724. doi:10.1175/BAMS-D-13-00179.1

Clements CB, Seto D (2015) Observations of fire–atmosphere interactions and near-surface heat transport on a slope. *Boundary-Layer Meteorology* **154**, 409–426. doi:10.1007/S10546-014-9982-7

Clements CB, Zhong S, Goodrick S, Li J, Bian X, Potter BE, Heilman WE, Charney JJ, Perna R, Jang M, Lee D, Patel M, Street S, Aumann G (2007) Observing the dynamics of wildland grass fires: FireFlux – field validation experiment. *Bulletin of the American Meteorological Society* **88**, 1369–1382. doi:10.1175/BAMS-88-9-1369

Clements CB, Zhong WS, Bian X, Heilman WE, Byun DW (2008) First observations of turbulence generated by grass fires. *Journal of Geophysical Research* **113**, D22102. doi:10.1029/2008JD010014

Coen JL, Cameron M, Michalakes J, Patton EG, Riggan PJ, Yedinak KM (2013) WRF-Fire: coupled weather–wildland fire modeling with the weather research and forecasting model. *Journal of Applied Meteorology and Climatology* **52**, 16–38. doi:10.1175/JAMC-D-12-023.1

Dee DP, Uppala SM, Simmons AJ, Berrisford P, Poli P, Kobayashi S, Andrae U, Balmaseda MA, Balsamo G, Bauer P, Bechtold P, Beljaars ACM, van de Berg L, Bidlot J, Bormann N, Delsol C, Dragani R, Fuentes M, Geer AJ, Haimberger L, Healy SB, Hersbach H, Hólm EV, Isaksen L, Kållberg P, Köhler M, Matricardi M, McNally AP, Monge-Sanz BM, Morcrette JJ, Park BK, Peubey C, de Rosnay P, Tavolato C, Thépaut JN, Vitart F (2011) The ERA-Interim Reanalysis: configuration and performance of the data assimilation system. *Quarterly Journal of the Royal Meteorological Society* **137**, 553–597. doi:10.1002/QJ.828

Dickinson MB, Hudak AT, Zajkowski T, Loudermilk EL, Schroeder W, Ellison L, Kremens RL, Holley W, Martinez O, Paxton A, Bright BC, O'Brien JJ, Hornsby B, Ichoku C, Faulring J, Gerace A, Peterson D, Mauceri J (2015) Measuring radiant emissions from entire prescribed fires with ground, airborne and satellite sensors – RxCADRE 2012. *International Journal of Wildland Fire* **25**, 48–61. doi:10.1071/WF15090

Filippi J-B, Pialat X, Clements CB (2013) Assessment of ForeFire/Meso-NH for wildland fire/atmosphere coupled simulation of the FireFlux experiment. *Proceedings of the Combustion Institute* **34**, 2633–2640. doi:10.1016/J.PROCI.2012.07.022

Horel JD, Dong X (2010) An evaluation of the distribution of remote automated weather stations (RAWS). *Journal of Applied Meteorology and Climatology* **49**, 1563–1578. doi:10.1175/2010JAMC2397.1

Hudak AT, Dickinson MB, Bright BC, Kremens RL, Loudermilk EL, O'Brien JJ, Hornsby B, Ottmar RD (2015) Measurements relating fire radiative energy density and surface fuel consumption – RxCADRE 2011 and 2012. *International Journal of Wildland Fire* **25**, 25–37. doi:10.1071/WF14159

Kochanski A, Jenkins M, Mandel J, Beezley J, Clements CB, Krueger S (2013) Evaluation of WRF-SFIRE performance with field observations from the FireFlux experiment. *Geoscientific Model Development* **6**, 1109–1126. doi:10.5194/GMD-6-1109-2013

Kremens RL, Dickinson MB (2015) Estimating radiated flux density from wildland fires using the raw output of limited-bandpass detectors. *International Journal of Wildland Fire* **24**, 461–469. doi:10.1071/WF14036

Ottmar RD, Hudak AT, Prichard SJ, Wright CS, Restaino JC, Kennedy MC, Vihnanek RE (2015) Pre-fire and post-fire surface fuel and cover measurements collected in the southeastern United States for model evaluation and development – RxCADRE 2008, 2011 and 2012. *International Journal of Wildland Fire* **25**, 10–24. doi:10.1071/WF15092

Pearson G, Davies F, Collier C (2009) An analysis of the performance of the UFAM pulsed Doppler lidar for observing the boundary layer. *Journal of Atmospheric and Oceanic Technology* **26**, 240–250. doi:10.1175/2008JTECHA1128.1

Pearson G, Davies F, Collier C (2010) Remote sensing of the tropical rain forest boundary layer using pulsed Doppler lidar. *Atmospheric Chemistry and Physics* **10**, 5891–5901. doi:10.5194/ACP-10-5891-2010

Potter BE (2012) Atmospheric interactions with wildland fire behaviour. Basic surface interactions, vertical profiles and synoptic structures. *International Journal of Wildland Fire* **21**, 779–801. doi:10.1071/WF11128

Silvani X, Morandini F (2009) Fire spread experiments in the field: temperature and heat fluxes measurements. *Fire Safety Journal* **44**, 279–285. doi:10.1016/J.FIRESAF.2008.06.004

Ware R, Carpenter R, Güldner J, Liljegren J, Nehrkorn T, Solheim F, Vandenberghe F (2003) A multichannel radiometric profiler of temperature, humidity, and cloud liquid. *Radio Science* **38**. doi:10.1029/2002RS002856

Zajkowski T, Dickinson MB, Hiers JK, Holley W, Williams B, Paxton A, Martinez O, Walker GW (2015) Evaluation and use of remotely piloted aircraft systems for operations and research – RxCADRE 2012. *International Journal of Wildland Fire* **25**, 114–127. doi:10.1071/WF14176